A numerical method to simulate hypersonic boundary layers with finite-rate chemistry

By O. Marxen, G. Iaccarino AND E. S. G. Shaqfeh

1. Motivation and objective

The accurate prediction of the location of laminar-turbulent transition in the boundary layer is a critical step in the design of hypersonic flight vehicles. Turbulent flow induces a much higher thermal load on the surface of vehicles re-entering a planetary atmosphere in comparison to laminar flow (Anderson 2000).

High temperatures affect the properties of the fluid, the flow, and hence the process of laminar-turbulent transition (Reed 2009). As temperature increases, the thermodynamic and transport properties of the gas, such as its specific heat and viscosity, are a function of temperature, and eventually for even higher temperature one might observe a dependence on both temperature and pressure owing to chemical reactions and barodiffusion in the gas mixture (Anderson 2000). The dissociating gas is in local thermodynamic and chemical equilibrium only if the characteristic time based on the flow velocity is large compared to all chemical reaction and thermal relaxation characteristic times. The gas composition then depends on only two thermodynamic quantities, such as the temperature and the pressure. The composition of a gas in chemical non-equilibrium, however, is governed by transport equations for the chemical species densities, and this complicates the numerical treatment significantly. The development of a numerical method applicable for the non-equilibrium regime is the main topic of this report.

The way high temperature gas effects influence boundary-layer dynamics may vary with the type of vehicle and its mission. For slender bodies at hypersonic speeds, the temperature at the boundary-layer edge may be comparable to the temperature of the environment through which the vehicle moves, owing to the small deflection angle of the leading edge shock produced by the vehicle. For these conditions, the temperature inside the boundary layer may be very high owing to a conversion of kinetic energy into thermal energy. For blunt re-entry vehicles, however, a strong increase in temperature is expected in the shock layer as a result of the severe bow shock in front of the vehicle. Hence, it is the edge temperature that may be highest in this case; for an example see figure 4 in Johnson & Candler (2010).

Studies of laminar-turbulent transition with a focus on high-temperature gas effects have mostly been based on experiments (Hornung 2006; Germain & Hornung 1997) or linear theories for parallel (Malik 2003; Johnson *et al.* 1998; Hudson *et al.* 1997; Stuckert & Reed 1994) and non-parallel flow (Johnson & Candler 2005). Theoretical approaches rely on numerical simulations in that they require a preceding computation of a steady-state flow, for which a number of low-order numerical methods exist (see for instance Liu & Vinokur 1989; Candler & Nompelis 2009).

Several numerical methods for finite-rate chemistry have been reported for flows involving combustion. While the expression 'finite-rate chemistry' is commonly used as a synonym for 'non-equilibrium chemistry' or 'real gas effects' in the literature on hypersonic flow, the combustion community uses the expressions 'detailed chemistry' or

'complete chemical scheme' instead. An overview of methods used for combustion is given in Hilbert *et al.* (2004). A number of second-order methods are described in the literature (Najm *et al.* 1998; Day & Bell 2000; Najm & Knio 2005), but only few method with higher order are reported (Nicoud 2000). All the cited methods have in common that they rely on a low Mach number formulation, and are therefore not applicable to the hypersonic flow regime.

Numerical simulations for hypersonic boundary layers are now routinely carried out if gas properties are assumed to be constant, i.e., if we have a calorically perfect gas. But not many numerical methods for non-equilibrium chemistry have been reported in which an unsteady solution to the compressible Navier-Stokes equations at hypersonic speeds has been sought (Zhong 1996; Kaneko *et al.* 2005; Stemmer 2005). The complexity associated with the combination of high Mach numbers, high temperatures, and unsteady boundary-layer transition makes such unsteady simulations challenging.

Numerical methods based on a high-order discretization are particularly well suited for simulations of unsteady transitional phenomena. These methods require low dispersion and dissipation in order to preserve the character of the underlying flow. Examples for these high-order numerical methods that are capable of handling the high-temperature regime including finite-rate chemistry can be found only in the recent literature, such as Duan & Martín (2009) and Parsons *et al.* (2010).

The state of boundary layer is strongly influenced by the conditions arising from vehicle geometry and its mission. The boundary layer could be in thermo-chemical equilibrium, chemical non-equilibrium and thermal equilibrium, or even in full thermo-chemical non-equilibrium including gas-surface interaction. For this reason, studies for all these conditions are justified at present. The condition of thermo-chemical equilibrium has previously been considered by Marxen *et al.* (2010*b*). In order to study the chemical non-equilibrium regime for complex, transitional test cases, a simulation code capable of handling this regime must be developed and verified. Reporting the development and verification of such a code is our goal here.

First, we will describe our approach of implementing a new numerical method based on a high-order finite-difference discretization for chemical non-equilibrium and thermal equilibrium. Then, two different simple verification test cases will be considered. Finally, the method will be applied to the case of a laminar boundary layer in chemical non-equilibrium.

2. Governing equations

The governing equations are the time-dependent three-dimensional Navier-Stokes equations for a compressible fluid in non-dimensional form. These equations are formulated for a mixture of thermally perfect gases in local thermal equilibrium, where chemical reactions are assumed to take place with a finite reaction rate, but vibrational relaxation occurs infinitely fast. In the following, the mathematical formulation for the mechanical motion of the fluid is given in section 2.1, while thermodynamic and transport closure aspects will be described in section 2.2.

2.1. *Equations of motion*

The Navier-Stokes equations are formulated for a gas with density ρ, temperature T, pressure p, and internal energy e. The velocity vector is given by $[\,u_1,\,u_2,\,u_3\,]^T = [\,u,\,v,\,w\,]^T$. It is a function of three spatial dimensions $[\,x_1,\,x_2,\,x_3\,]^T = [\,x,\,y,\,z\,]^T$ and time t. Non-dimensionalization is based on the freestream conditions (marked by $_\infty$), and the follow-

ing reference quantities are chosen: a reference temperature $\tilde{T}_{ref} = (\gamma_\infty - 1)\tilde{T}_\infty$, density $\tilde{\rho}_\infty$, specific heat ratio γ_∞=$\tilde{c}_{p,\infty}/\tilde{c}_{v,\infty}$, thermal conductivity $\tilde{k}_\infty$, and viscosity $\tilde{\mu}_\infty$ (all dimensional quantities are marked by the modifier $\tilde{}$). The reference velocity is the speed of sound $\tilde{c}_\infty$, and we have chosen a reference length $\tilde{L}_{ref}$. For the geometries considered in this report, no obvious length scale is present and hence the choice of the reference length is arbitrary. The chosen quantities yield a reference time $\tilde{t}_{ref} = \tilde{L}_{ref}/\tilde{c}_\infty$ and a reference pressure $\tilde{p}_{ref} = \tilde{\rho}_\infty \tilde{c}_\infty^2$. This results in the following set of non-dimensional equations for total mass, species mass, momentum and energy conservation for NS species:

$$\frac{\partial \rho}{\partial t} + \frac{\partial}{\partial x_j}\left(\rho u_j\right) = 0, \tag{2.1}$$

$$\frac{\partial \rho^s}{\partial t} + \frac{\partial}{\partial x_j}\left(\rho^s u_j + J_j^s\right) = \dot{w}^s, \quad s = 1 \ldots NS \tag{2.2}$$

$$\frac{\partial (\rho u_i)}{\partial t} + \frac{\partial}{\partial x_j}\left(\rho u_i u_j + p\delta_{ij}\right) = \frac{\partial \sigma_{ij}}{\partial x_j}, \quad i = 1, 2, 3, \tag{2.3}$$

$$\frac{\partial E}{\partial t} + \frac{\partial}{\partial x_j}\left[\left(E + p\right) u_j\right] = -\frac{\partial q_j}{\partial x_j} + \frac{\partial}{\partial x_k}\left(u_j \sigma_{ij}\right). \tag{2.4}$$

The total energy E per unit volume, the viscous stress tensor σ_{ij} and the heat flux vector q_j are defined as

$$E = e\rho/Ec_\infty + \frac{1}{2}\rho u_i u_i, \tag{2.5}$$

$$\sigma_{ij} = \frac{\mu}{Re_\infty}\left(\frac{\partial u_i}{\partial x_j} + \frac{\partial u_j}{\partial x_i} - \frac{2}{3}\frac{\partial u_k}{\partial x_k}\delta_{ij}\right), \tag{2.6}$$

$$q_j = \frac{-1}{Re_\infty Pr_\infty Ec_\infty} k \frac{\partial T}{\partial x_j} + \sum_{s=1\ldots NS} h^s J_j^s. \tag{2.7}$$

In the last equation, k is the thermal conductivity and h^s the enthalpy for species s. The diffusion flux J_j^s will be specified in section 2.2. The Reynolds number Re_∞, Prandtl number Pr_∞, and Eckert number Ec_∞ are

$$Re_\infty = \tilde{\rho}_\infty \tilde{c}_\infty \tilde{L}_{ref}/\tilde{\mu}_\infty, \quad Pr_\infty = \tilde{\mu}_\infty \tilde{c}_{p,\infty}/\tilde{k}_\infty, \tag{2.8}$$

$$Ec_\infty = \tilde{c}_\infty^2 / \left(\tilde{c}_{p,\infty}\left(\gamma_\infty - 1\right)\tilde{T}_\infty\right). \tag{2.9}$$

The Mach number M_∞ is computed with the streamwise velocity in the freestream $\tilde{u}_\infty$ and the speed of sound $\tilde{c}_\infty$, i.e., $M_\infty = \tilde{u}_\infty/\tilde{c}_\infty$. The choice of reference quantities results in a unity Eckert number for a calorically perfect gas. Throughout this report, we will provide only the dimensionless numbers with the exception of the temperature $\tilde{T}_\infty$ and the density $\tilde{\rho}_\infty$.

2.2. *High-temperature gas model*

Within this report we assume that the gas consists of a mixture of perfect gases in local thermodynamic equilibrium. The internal energy e of the gas is computed as the sum of contributions from all species s:

$$e = -\frac{p}{\rho} + \sum_s \chi^s h^s. \tag{2.10}$$

In this equation, h^s contains the heat of formation for species s, respectively. Quantity $\chi^s = \rho^s/\rho$ stands for the species mass fraction.

Internal energy and the species densities can be used to compute the temperature $\tilde{T}$:

$$T = \tilde{T}(\tilde{e}, \tilde{\rho}^s) / \left((\gamma - 1) \tilde{T}_\infty \right) . \tag{2.11}$$

The temperature can be used to obtain the pressure $\tilde{p}$:

$$p = \tilde{p}(\tilde{T}, \tilde{\rho}, \chi^s) / \left(\tilde{\rho}_\infty \tilde{c}_\infty^2 \right) . \tag{2.12}$$

Similarly, transport properties are computable, viz,

$$k = \tilde{k}(\tilde{e}, \tilde{\rho}^s) / \tilde{k}_\infty , \tag{2.13}$$

$$\mu = \tilde{\mu}(\tilde{e}, \tilde{\rho}^s) / \tilde{\mu}_\infty . \tag{2.14}$$

The computation of species source term also involves molar mass of species s, M^s:

$$\dot{w}^s = M^S \tilde{\omega}(\tilde{e}, \tilde{\rho}^s) / \left(\tilde{\rho}_\infty \tilde{L}_{ref} / \tilde{c}_\infty \right) . \tag{2.15}$$

In addition to the input quantities used in Eqs. (2.11) to (2.15), the computation of diffusion flux also requires concentration gradients, i.e., $\partial \chi^s / \partial \tilde{x}_j$:

$$J_j^s = \tilde{J}_j^s (\partial \chi^s / \partial \tilde{x}_j, \tilde{T}, \tilde{p}, \tilde{\rho}, \tilde{\rho}^s) / \left(\tilde{\rho}_\infty \tilde{c}_\infty \right) . \tag{2.16}$$

Thermodynamic gas and transport properties as well as chemical reaction rates, given in Eqs. (2.11) to (2.16), are computed by the MUTATION library, which is called by the flow solver. A detailed description of the physio-chemical model underlying the MUTATION library can be found in Magin & Degrez (2004) and Barbante & Magin (2004). Calls to the MUTATION library are performed within the flow solver, i.e., the Navier-Stokes code.

Within a subroutine of the MUTATION library, Eq. (2.11) is solved iteratively. The resulting temperature then is used to obtain the pressure. Next, mole fractions, number densities and collision integrals are computed. These quantities are required to compute the viscosity and the total thermal conductivity by means of a Krylov method. All quantities handed over to the library are dimensional, and so are the results handed back, which have to be non-dimensionalized before they can be used in the Navier-Stokes code. For performance reasons, the temperature is saved from the previous RK substep and is used as an initial guess for the iterative solution of Eq. (2.11) at the next step. The diffusion flux J_j^s, Eq. (2.16), is computed separately after an evaluation of concentration gradients $1/\tilde{L}_{ref}\, \partial \chi^s / \partial x_j$.

2.3. *Numerical method*

The basis for the numerical method applied here is an algorithm described in Nagarajan *et al.* (2003). It was originally developed for transitional flow in subsonic conditions (Nagarajan *et al.* 2007), but has since been modified and applied to supersonic conditions (Marxen *et al.* 2010*a*).

Time- and space-accurate solutions are obtained based on sixth-order compact finite-differences in the interior of the domain with explicit third-order Runge-Kutta (RK) time stepping. The numerical discretization is constructed on a structured, Cartesian grid using staggered variables.

In streamwise direction, the grid is given by an equidistant spacing in x direction with NX points. In y direction, a grid stretching can be applied using MY points.

No. of species NS / gas	Re_∞	Pr_∞	γ_∞	M_∞	$\tilde{T}_\infty$
5 / air: N, O, N_2, NO, O_2	10^4	0.69	1.397	10	350 K

TABLE 1. General parameters for test cases considered here.

$\tilde{T}$	$\tilde{\rho}$	χ^N	χ^O	χ^{N_2}	χ^{NO}	χ^{O_2}
$5918.87\,K$	$0.255537 \cdot 10^{-2}\,kg/m^3$	0	0	0.767082	0	0.232918

TABLE 2. Postshock conditions ($x = 0$), test case of section 3.1.

3. Verification

The simulation code has been used previously to compute reacting flow in chemical equilibrium (Marxen *et al.* 2010*b*). The computation of pressure, Eq. (2.12), and viscosity, Eq. (2.14), remains the same as in the implementation for chemical equilibrium. The computation of temperature, Eq. (2.11), is slightly different, since the equilibrium composition no longer needs to be determined simultaneously with the temperature. Nor does the thermal conductivity, Eq. (2.13), need to account for the effect of change in composition on the heat flux. In the equilibrium case considered by Marxen *et al.* (2010*b*), this effect was captured by using an equivalent thermal conductivity for conditions in chemical equilibrium. Nevertheless, these changes were deemed to be minor, so all quantities given in Eqs. (2.11) to (2.14) were not tested separately. Their correct implementation will, however, be essential for one or the other of the verification test cases discussed below.

In contrast, the implementation of Eq. (2.15), and the appearance of $\dot{w}^s$ in the species continuity Eq. (2.2) have not been part of any previous implementation. A specific check has therefore been carried out and will be reported below in section 3.1. Similarly, the verification of computing the diffusion flux J_j^s, Eq. (2.16), and its incorporation into the heat flux Eq. (2.7) has been checked and will be treated in section 3.2. If the computation of diffusion flux is found to match reference results, we can assume that the corresponding term appearing in the species continuity Eq. (2.2) is also correct. Therefore, we did not perform a separate check targeting the term $\partial J_j^s/\partial x_j$ in this equation. We note, however, that this term was active in the test case reported in section 3.2, but remained small and did not significantly influence the solution.

Both test cases consider almost identical conditions, as given in Table 1. The integration domain and the freestream density were different in the two cases and will be specified below.

3.1. *Species source term*

In order to verify the species source term obtained from Eq. (2.15), we have selected the one-dimensional flow field behind a normal shock wave. Conditions given in Table 1 correspond to conditions upstream of the shock, with a density upstream of the shock with the value $\tilde{\rho}_\infty = 0.3565 \cdot 10^{-3}\,kg/m^3$. The shock is located at the origin of the coordinate system. Quantities immediately behind the shock were obtained using the SHOCKING code (for a description and validation, see Magin *et al.* 2006). These quantities are specified in Table 2 and were prescribed as inflow (and initial) condition for a simulation using our new implementation, and then the flow field was progressed in time until a steady state was reached. In this simulation, the diffusion flux has been set to zero, i.e., $J_j^s \equiv 0$.

Even though this test case consists of a one-dimensional setup, the actual computa-

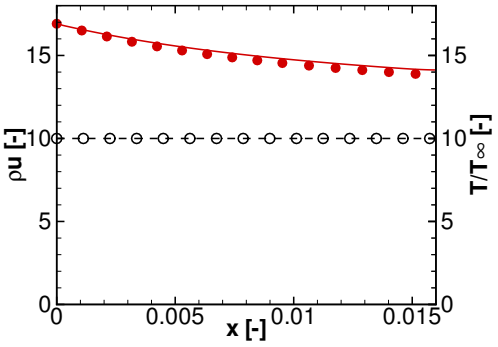

FIGURE 1. Flow quantities (from top to bottom: temperature $\tilde{T}/\tilde{T}_\infty$, streamwise momentum ρu) computed using the SHOCKING code (symbols) and present result (lines).

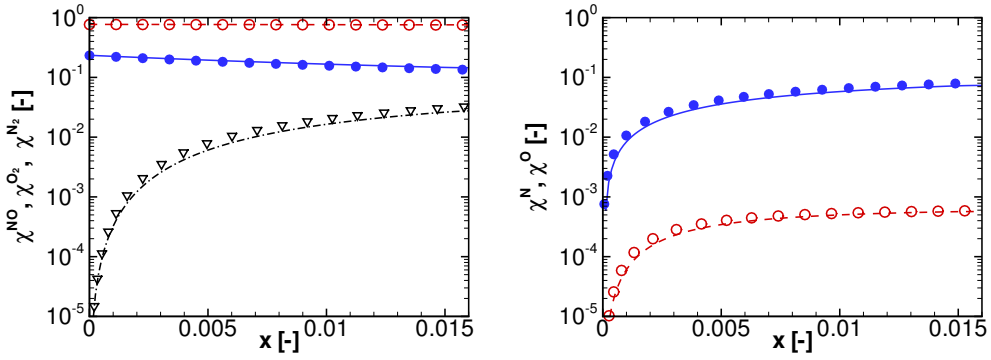

FIGURE 2. Species mass fractions $\chi^s = \rho^s/\rho$ computed using the SHOCKING code (symbols) and present result (lines). Left: molecular quantities (from top to bottom: s=N_2, O_2, NO). Right: atomic quantities (from top to bottom: s=O, N).

tions were performed in two dimensions. The integration domain extended from right behind the shock, $x = 0$, to $x = 0.02$ using 160 grid points in streamwise dimension. In y direction, 21 grid points have been used within the interval $y \in [0, 0.05]$. Periodic boundary conditions have been applied in y direction.

Simulation results are depicted in Figures 1 & 2, where they are also compared to results obtained with the SHOCKING code downstream of the shock location. A good agreement is found for flow quantities (Figure 1) as well as species concentrations (Figure 2). This verifies our implementation of the species source term.

3.2. *Diffusion flux*

In order to check the diffusion flux J_j^s, Eq. (2.16), and its incorporation into the heat flux Eq. (2.7) we will consider a case which has been used in Marxen *et al.* (2010*b*).

This case considers the flow over a flat plate in local thermo-chemical equilibrium with a freestream velocity $u_\infty = u(y_2) = M_\infty$. A very similar setup has been used by Marxen *et al.* (2007), and it was based on an investigation reported in Malik & Anderson (1991). The origin of the coordinate system is located at the leading edge of the flat plate. The computational domain is placed downstream of this (virtual) leading edge. At the inflow

x_1	x_2	y_1	y_2	NX	MY
11.6065	68.7265	0.0	1.575	400	51

TABLE 3. Parameters determining integration domain and resolution, test case of section 3.2.

x_1, a self-similar boundary-layer solution is prescribed while the wall boundary condition (B.C.) at y_1 for the mean flow is adiabatic with a no-slip condition. A non-catalytic condition has been used for the species densities, i.e., $\partial\rho^s/\partial y = 0$. Within a certain region close to the inflow x_1, the outflow x_2, and in the freestream y_2, the solution is damped towards the corresponding laminar, self-similar state (sponge region). In wall-normal direction, a grid stretching is applied, with the following formula holding at all streamwise locations n, with κ=0.5 and m=1 ... MY:

$$y(n,m) = y_1 \left((1-\kappa) \left(\frac{m-1}{MY-1} \right)^3 + \kappa \frac{m-1}{MY-1} \right). \tag{3.1}$$

The coefficients appearing in this equation, together with the streamwise and wall-normal resolution, are specified in Table 3. Motivated by our interest in the laminar steady-state solution only, we have used a lower resolution in x and y as compared to Marxen *et al.* (2010*b*).

The freestream density amounts to $\tilde{\rho}_\infty = 0.3565 \cdot 10^{-1}\, kg/m^3$. The initial flow field was set to be the flow field in chemical equilibrium. In order to ensure that the flow remains in a chemical equilibrium at all times, we have replaced the species source term, Eq. (2.15), by the following expression:

$$\dot{w}^s = -\lambda \left(\rho^s - \rho^s_{eq} \right) . \tag{3.2}$$

In this equation, λ is a large number (here: 10^4) and ρ^s_{eq} is the species density that we would see for the given total density ρ and energy e if we had thermo-chemical equilibrium (at the respective point in space). The quantity $\rho^s_{eq} = \rho\, \chi^s_{eq}$ is based on an expression similar to Eq. (2.11), but using the additional constraint of equilibrium and feeding in only the total density instead of the species densities:

$$\chi^s_{eq} = \chi^s(\tilde{e}, \tilde{\rho})\,|_{eq} \ . \tag{3.3}$$

Eq. (3.3) is solved iteratively using the MUTATION library. Technically, the routine to determine the temperature under the assumption of local thermo-chemical equilibrium, which has been used previously for runs in chemical equilibrium mode, is employed to obtain χ^s_{eq}. This routine provides the equilibrium composition χ^s_{eq} as an output in addition to the temperature.

Results are depicted in Figure 3. In this figure, these results are compared to the corresponding self-similar simulation (which also served as an initial condition), confirming that the Navier-Stokes solution does indeed stay close to the self-similar solution. The largest difference (10%) can be observed for the wall-normal velocity v in the free stream. Compared to the streamwise velocity u, the difference for v is magnified due to multiplication with the local Reynolds number Re_x. Moreover, unlike the self-similar solution, the Navier-Stokes solution v is not constant along y in the free stream, but increases with increasing y. A similarly good agreement was seen at other streamwise locations.

In order to demonstrate that the diffusion flux J^s_j has a non-negligible effect on the simulation results, we repeated the simulation while setting this term to zero, i.e., $J^s_j \equiv 0$. It is clear that in this case, not only do we obtain the wrong composition close to the

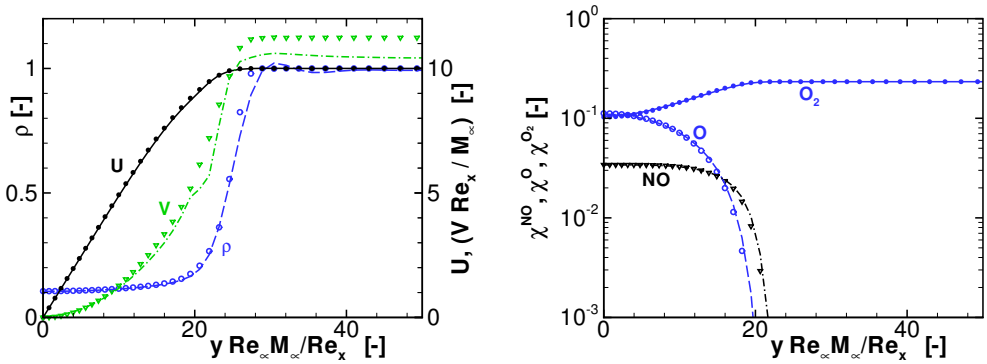

FIGURE 3. Results at $Re_x = 2000$ for the self-similar solution (symbols) and from numerical simulation (lines). Left: boundary-layer profiles. Right: species mass fractions $\chi^s = \rho^s/\rho$.

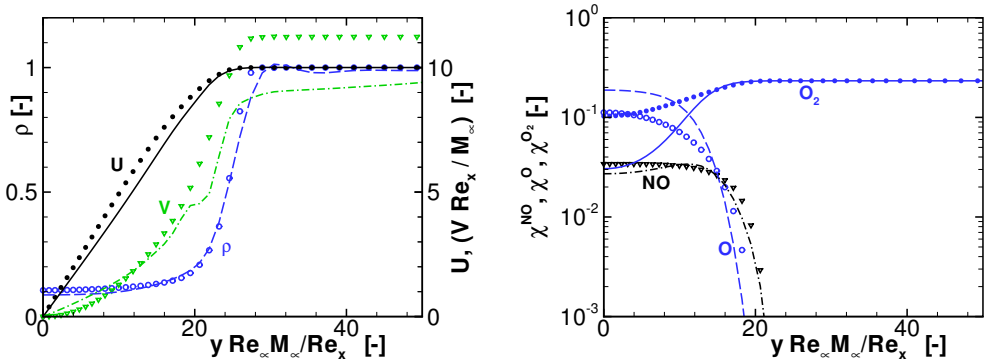

FIGURE 4. Results at $Re_x = 2000$ for the self-similar solution (symbols) and from numerical simulation for which the diffusion term has been switched off, i.e., $J_j^s \equiv 0$ (lines). Left: boundary-layer profiles. Right: species mass fractions $\chi^s = \rho^s/\rho$.

wall as seen in Figure 4 (right), but also the velocity profiles are slightly different Figure 4 (left).

4. Simulation results for a non-equilibrium reacting laminar boundary layer

For a simulation of a reacting laminar boundary layer in non-equilibrium we consider the same setup as in section 3.2, i.e., a flat-plate boundary layer with adiabatic wall. However, in contrast to section 3.2, we now allow for finite-rate chemistry, and the integration domain starts close to the leading edge. To avoid numerical problems caused by the leading edge singularity, the inflow boundary is placed slightly downstream of the nominal leading edge. The domain size was $x \in [0.025, 2.4]$ and $y \in [0, 0.375]$, with $MX = 160$ and $MY = 101$. Grid stretching is applied in both the streamwise and the wall-normal direction ($\kappa = \kappa_y = 0.5$ in Eq. (3.1) and $\kappa_x = 0.25$ using an analogous equation for x). The composition χ^s at the inflow was the same as the one given in Table 2.

A visualization of the flow field is given in Figure 5. The depiction of the streamwise

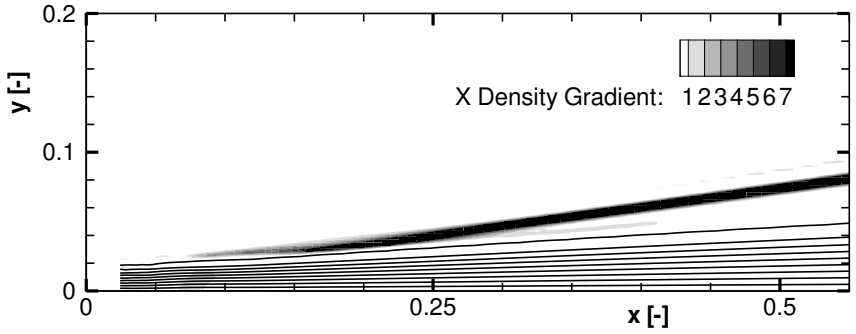

FIGURE 5. Visualization of the flow in the vicinity of the leading edge: contours of streamwise density gradient (gray scale) and contours of the streamwise velocity (lines, levels $1.1 \ldots 9.1, \Delta = 1.1$).

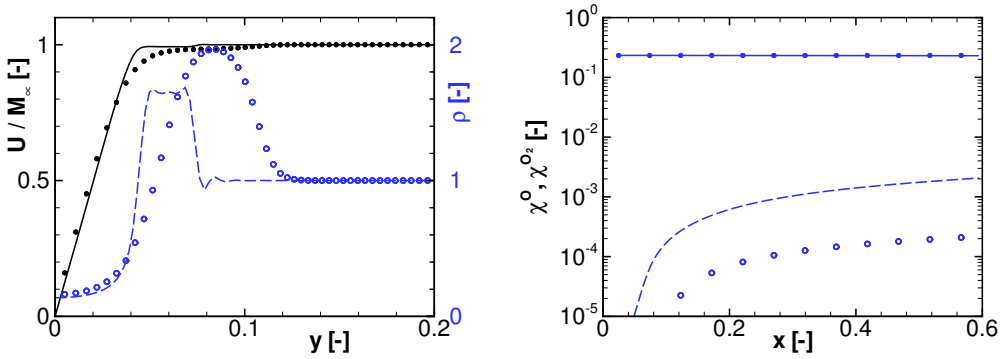

FIGURE 6. Comparison between results of Franko *et al.* (2010) (symbols) and present numerical simulation (lines). Left: boundary-layer profiles at x=0.5 (solid line / filled symbols: u/Ma_∞; dashed line / open symbols: ρ). Right: species mass fractions $\chi^s = \rho^s/\rho$ at the wall (from top to bottom: $s = O_2, O$).

density gradient reveals that due to the initially strong growth of the boundary layer, an oblique shock wave starts close to the inflow boundary.

A similar setup was considered by Hudson *et al.* (1997), and more recently by Franko *et al.* (2010). However, in contrast to our setup, the freestream temperature in their case was only $\tilde{T}_\infty = 278\,K$, and the inflow boundary was located at $x = 0$ with a uniform flow (freestream conditions) prescribed at their inflow boundary. Moreover, the temperature in a region close to the wall at the inflow is much higher in our case. Due to these differences, a perfect match of their results cannot be expected when compared to our simulation data. Nevertheless, the agreement as seen in Figure 6 is reasonably good. However, there is a considerable difference in the location and thickness of the shock as visible from the negative density gradient in Figure 6 (left) and in the onset of chemical reactions, which start closer to the leading edge in our case. Chemical reactions set in earlier in our case possibly due to the higher temperature prescribed at the inflow in our case, but maybe also due to a finer grid that we used in the streamwise direction.

5. Conclusions

An existing numerical method for the direct numerical simulation of hypersonic boundary layers has been extended to handle chemically reacting gas with finite reaction rates. The code applies high-order finite differencing and explicit time stepping to the compressible Navier-Stokes equations. The corresponding fluid consists of a mixture of chemically reacting gases with, in principle, an arbitrary number of species. The new implementation relies on a coupling of a fluid dynamics part of the simulation code with the MUTATION library for transport properties and chemistry. The extension of the code was based on a previously developed and tested version capable of handling equilibrium chemistry. This extension consists of an additional set of transport equations for each species and an additional diffusion term in the energy equation.

Two different verification test cases have been considered, both of which use air modeled by five species. The first test is a one-dimensional subsonic case. The purpose of this case is to check the chemical source term, and a very good agreement with results obtained by a different code has been observed. The second test is a two-dimensional hypersonic boundary layer in local thermo-chemical equilibrium, whose purpose is to test the diffusion terms. Again, the verification has been successful. Finally, a laminar hypersonic boundary layer in non-equilibrium has been simulated and compared against results obtained with a code that used the same gas model, but a different solution procedure for the fluid dynamics part. Reasonable, though not perfect agreement was observed, and potential reasons for the differences seen have been suggested.

6. Future work

The inflow condition for the simulation of a laminar hypersonic boundary layer in non-equilibrium reported here needs to be altered in order to improve the agreement with the results of Franko *et al.* (2010). Then, the simulation will need to be extended to capture a significantly longer domain in the downstream direction. For such a longer domain, it is planned to investigate the evolution of a small-amplitude disturbance in the reacting boundary layer and compare the amplification to the case of chemical equilibrium. In our present formulation, integrating both the total mass conservation equation and all species conservation equations did not pose any problems, but should be avoided since it is an overspecification of the system of equations. An investigation of possible solutions to this issue, including not solving a transport equation for the total density, is ongoing.

7. Acknowledgments

Financial support from the National Aeronautics and Space Administration (NASA) under grant #NNX07AC29A is gratefully acknowledged. The authors acknowledge the High Performance Computing Center at Stanford University for providing computing resources. OM would like to thank T. Magin, VKI Brussels, for his help in implementing the coupling of the Navier-Stokes code to the MUTATION library. We are grateful to S. Lele and K. Franko, Stanford University, for useful discussions and providing the simulation data used for comparison here, and to J. Nichols and to S. Ghaffari, Stanford University, for insightful discussions. We would like to thank A. Lani, Stanford University, for valuable comments on this manuscript.

REFERENCES

Anderson, J. D. 2000 *Hypersonic and High Temperature Gas Dynamics*. AIAA.

Barbante, P. F. & Magin, T. E. 2004 Fundamentals of hypersonic flight – Properties of high temperature gases. In *RTO-EN-AVT-116 Critical Technologies for Hypersonic Vehicle Development*, pp. 5.1–5.50. van Karman Institut, Rhode-Saint-Genese, Belgium.

Candler, G. V. & Nompelis, I. 2009 Computational fluid dynamics for atmospheric entry. In *RTO-EN-AVT-162 Non-Equilibrium Gas Dynamics – From Physical Models to Hypersonic Flights*, pp. 15.1–15.56. van Karman Institut, Rhode-Saint-Genese, Belgium.

Day, M. S. & Bell, J. B. 2000 Numerical simulation of laminar reacting flows with complex chemistry. *Combust. Theor. Model.* **4**, 535–556.

Duan, L. & Martín, M. P. 2009 Procedure to validate direct numerical simulations of wall-bounded turbulence including finite-rate reactions. *AIAA J.* **47** (1), 244–251.

Franko, K. J., MacCormack, R. W. & Lele, S. K. 2010 Effects of chemistry modeling on hypersonic boundary layer linear stability prediction. *AIAA Paper 2010–4601*.

Germain, P. D. & Hornung, H. G. 1997 Transition on a slender cone in hypervelocity flow. *Exp. Fluids* **22**, 183–190.

Hilbert, R., Tap, F., El-Rabii, H. & Thèvenin, D. 2004 Impact of detailed chemistry and transport models on turbulent combustion simulations. *Prog. Energ. Combust.* **30** (1), 61 – 117.

Hornung, H. G. 2006 Hypersonic real-gas effects on transition. In *IUTAM Symposium on One Hundred Years of Boundary Layer Research* (ed. G.E.A. Meier & K.R. Sreenivasan), pp. 335–344. Springer, The Netherlands.

Hudson, M. L., Chokani, N. & Candler, G. V. 1997 Linear stability of hypersonic flow in thermochemical nonequilibrium. *AIAA J.* **35** (6), 958–964.

Johnson, H. B. & Candler, G. V. 2005 Hypersonic boundary layer stability analysis using PSE-Chem. *AIAA Paper 2005-5023* .

Johnson, H. B. & Candler, G. V. 2010 Orbiter boundary layer stability analysis at flight entry conditions. *AIAA Paper 2010–457* .

Johnson, H. B., Seipp, T. & Candler, G. V. 1998 Numerical study of hypersonic reacting boundary layer transition on cones. *Phys. Fluids* **10** (10), 2676–2685.

Kaneko, M., Men'shov, I. & Nakamura, Y. 2005 Numerical simulation of nonequilibrium flow in high-enthalpy shock tunnel. *Energy* **30** (2-4), 165 – 179.

Liu, Y. & Vinokur, M. 1989 Nonequilibrium flow computations. I. An analysis of numerical formulations of conservation laws. *J. Comput. Phys.* **83**, 373–397.

Magin, Thierry E., Caillault, L., Bourdon, A. & Laux, C. O. 2006 Nonequilibrium radiative heat flux modeling for the Huygens entry probe. *J. Geophys. Res* **111** (E07S12), 1–11.

Magin, Thierry E. & Degrez, Gérard 2004 Transport algorithms for partially ionized and unmagnetized plasmas. *J. Comput. Phys.* **198** (2), 424–449.

Malik, M. R. 2003 Hypersonic flight transition data analysis using parabolized stability equations with chemistry effects. *J. Spacecraft Rockets* **40** (3), 332–344.

Malik, M. R. & Anderson, E. C. 1991 Real gas effects on hypersonic boundary-layer stability. *Phys. Fluids A* **3** (5), 803–821.

Marxen, O., Iaccarino, G. & Shaqfeh, E. 2007 Numerical simulation of hypersonic instability using different gas models. In *Annual Research Briefs 2007*. Center for Turbulence Research, Stanford University.

Marxen, O., Iaccarino, G. & Shaqfeh, E. 2010*a* Disturbance evolution in a Mach 4.8 boundary layer with two-dimensional roughness-induced separation and shock. *J. Fluid Mech.* **648**, 435–469.

Marxen, O., Magin, T., Iaccarino, G. & Shaqfeh, E. 2010*b* Hypersonic boundary-layer instability with chemical reactions. *AIAA Paper 2010–707* .

Nagarajan, S., Lele, S. K. & Ferziger, J. H. 2003 A robust high-order method for large eddy simulation. *J. Comput. Phys.* **191**, 392–419.

Nagarajan, S., Lele, S. K. & Ferziger, J. H. 2007 Leading-edge effects in bypass transition. *J. Fluid Mech.* **572**, 471–504.

Najm, H. & Knio, O. 2005 Modeling low Mach number reacting flow with detailed chemistry and transport. *J. Sci. Comput.* **25**, 263–287, 10.1007/BF02728991.

Najm, H. N., Wyckoff, P. S. & Knio, O. M. 1998 A semi-implicit numerical scheme for reacting flow. I. Stiff chemistry. *J. Comput. Phys.* **143**, 381–402.

Nicoud, F. 2000 Conservative high-order finite-difference schemes for low-mach number flows. *J. Comput. Phys.* **158** (1), 71–97.

Parsons, N., Zhong, X., Kim, J. & Eldredge, J. 2010 Numerical study of hypersonic receptivity with thermochemical non-equilibrium on a blunt cone. *AIAA Paper 2010–4446* .

Reed, H. 2009 Role of chemical reactions in hypersonic flows. In *RTO-EN-AVT-151 Advances in Laminar-Turbulent Transition Modelling*, pp. 13.1–13.15. van Karman Institut, Rhode-Saint-Genese, Belgium.

Stemmer, C. 2005 Hypersonic transition investigations in a flat-plate boundary-layer flow at M=20. *AIAA Paper 2005–5136* .

Stuckert, G. & Reed, H. L. 1994 Linear disturbances in hypersonic, chemically reacting shock layers. *AIAA J.* **32** (7), 1384–1393.

Zhong, Xiaolin 1996 Additive semi-implicit Runge-Kutta methods for computing high-speed nonequilibrium reactive flows. *J. Comput. Phys.* **128** (1), 19 – 31.